A Novel Acid-Base Catalyzed Sol-Gel Synthesis of Highly Active Mesoporous TiO₂ Photocatalysts[†]

Romana Khan, Sun Woo Kim, Tae-Jeong Kim,[*] and Hyosun Lee[‡]

Department of Applied Chemistry, Kyungpook National University, Daegu 702-701, Korea. [*]E-mail: tjkim@knu.ac.kr
[‡]Department of Chemistry, Kyungpook National University, Daegu 702-701, Korea

A new synthetic strategy based on the acid-base catalyzed sol-gel method was developed for the preparation of a series of mesoporous TiO₂ nanoparticles. A key feature of the method involves a gradual change in pH (0.8-9) during the sol-gel transition, which guarantees easy introduction of mesoporosity without relying on the well-established sonochemical or template approach. In addition, this method leads to the exclusive formation of the anatase phase stable enough to the calcination temperature up to 600 °C. The physicochemical properties of the particles in the series were characterized by various spectroscopic and analytical techniques such as wide-angle XRD, SAXRD, BET surface area, FE-SEM, TEM, FT-IR, TGA, and XPS. The photocatalytic efficiency of these materials was investigated for the oxidation of toluene under UV-irradiation. All but T-ad in the series exhibited high photocatalytic activity pushing the reaction into completion within 3 h. The reaction followed the first order kinetics, and the rate reaches as high as 3.9×10^{-2}/min which exceeds the one with the commercially available Degussa P-25 by a factor of 3.2. When comparison is made among the catalysts, the reactivity increases with increase in the calcination temperature which in turn increases the crystallinity of the anatase phase, thus revealing the following rate orders: T-3 < T-4 < T-5 < T-6.

Key Words : Photocatalyst, TiO₂, Sol-gel, Mesoporous, Toluene degradation

Introduction

The environmental pollution is a serious global concern. The semiconductor-mediated photocatalytic decontamination of air and water is a promising environmental remediation technology because fewer chemicals are required and complete mineralization is possible at room-temperature.[1] Of various known oxide semiconductors, TiO₂ is the most widely used photocatalyst because of its strong redox power, high photocorrosion resistance, nontoxicity and cost effectiveness. The photocatalytic activity of TiO₂ depends on certain physical properties such as crystallinity, crystal phase, phase stability, crystallite size, specific surface area and mesoporosity.[2-7]

These physical characteristics in turn depend on the method of preparation and reaction conditions. Among various synthetic methods, the sol-gel method is believed to be the most suitable approach for the synthesis of TiO₂. This technique is especially valuable because the physical and chemical properties of the final solid can be tuned throughout the whole process. Additionally, this process is simple and easy to obtain the product in a pure form and in large quantities.[8,9]

In a sol-gel process, two simultaneous reactions such as hydrolysis and condensation take place. The overall reaction rates can be monitored by controlling various experimental parameters such as the types and concentrations of both acid and base catalysts, the types of solvent, the amount of water, and the reaction temperature. Extensive studies have led to the conclusions that water and the catalyst are two most important factors. They are known to control not only the reaction rates but also the properties of the final product.[10-14] The traditional sol-gel methods have so far employed only one type of catalyst, HCl or NH₄OH. Yet, each catalyst has both advantages and drawbacks of its own. For instance, although the acid catalysis with HCl leads to the formation of a smaller particle size, larger surface area, and lower aggregation, it nevertheless results in a mixture of anatase and brookite (or rutile) phases. The anatase phase produced under this condition exhibit reduced stability by undergoing the anatase-rutile transformation at the temperature as low as 400 °C. Further, the acid catalysis with an excess amount of HCl leads only to the formation of microporous structure. The base catalysis, on the other hand, results in the mesoporous structure. However, the resulting powders are amorphous and thus require higher calcination temperature for crystallization, during which process the shape of mesopores is diminished. Another drawback in connection with the base catalysis is that it yields a larger crystallite size, smaller surface area, and higher aggregation.[15-19]

Judging from these observations, a proper combination of both catalyses would be strongly recommended in order to obtain such physicochemical properties as required for high photocatalytic activity. We have thus designed a new acid-base catalyzed sol-gel process for the preparation of a series of mesoporous TiO₂ powders at an ambient temperature. Indeed, TiO₂ thus prepared shows crystallinity constituting of anatase as a sole phase on drying. Furthermore, various other improvements have also been noted such as a large surface area, small particle sizes, and high phase stability.

Most significant of all, these particles exhibit higher reactivity than that of commercially available Degussa P-25 in the photocatalytic activation of toluene under UV irradiation. These observations along with their synthesis and characterization will be presented in this paper.

Experimental

Materials. All commercial reagents were purchased from Aldrich and used as received.

Preparation of TiO₂. To a solution of titanium butoxide (26.4 mL, 0.077 mol) in absolute ethanol (175 mL, 3.00 mol) was added drop wise a mixture of deionized water (26.4 mL, 1.50 mol), hydrochloric acid (8 mL, 0.096 mol) and absolute ethanol (175 mL, 3.00 mol). The initial transparent solution turned to a stable, opaque sol in 12 h. After stirring for an additional 12 h, ammonium hydroxide (1.0 M) was added drop wise until pH of the solution rose to 9.0. The solution was then left standing for 2 h during which time gelation took place through a sequence of hydrolysis and polycondensation reactions. The gel thus formed was filtered out through a sintered glass funnel and washed thoroughly with water to remove ammonium chloride. The complete removal of chloride ions was confirmed by the silver nitrate test. The gel was dried at 110 °C for 12 h. The light yellow xerogel transformed into white powders (T-ad) when subjected to mechanical grinding. The sample was then calcined at various temperatures from 350 °C to 800 °C for 5 h at the rate of 1 °C per minute in air to yield a series of TiO₂ nanoparticles with varying sizes: (i) T-3 (350 °C); (ii) T-4 (400 °C); (iii) T-5 (500 °C); (iv) T-6 (600 °C); (v) T-8 (800 °C).

Characterization. XRD measurements were carried out with a Multi-Purpose X-ray Diffractometer (X'pert PRO MRD/X'pert PRO MPD) operated at room temperature with graphite-monochromated Cu Kα radiation. The morphology of the samples was examined by means of scanning electron microscopy (SEM, Hitachi, S-4300) and a high-resolution transmission electron microscope (HRTEM) (model: JEOL, JEM 3010) operated at 300 kV. For TEM images, a drop of a dilute dispersion was deposited on a copper grid covered with a formal-carbon membrane. Specific surface area measurements were performed using a BET Surface Area Analyzer (Micrometrics, Pore sizer 9320). The texture properties of the samples were determined through nitrogen adsorption at 77 K. The specific surface area was determined by the multipoint BET method using the adsorption data in the relative pressure (P/P0) range of 0-1. The desorption isotherm was used to determine the pore size distribution using the Barrett, Joyner, and Halenda (BJH) method. Thermal gravimetric analysis (TGA) was performed using a thermogravimetric/differential thermal analyzer (Seiko Instruments Inc.) in the range of 30-1000 °C under a nitrogen atmosphere with a temperature increase of 20 °C min⁻¹. X-ray photoelectron spectra (XPS) were recorded on a VG Microtech, MT 500/1 photoelectron spectrometer. FT-IR spectra of the samples were obtained using a Mattson
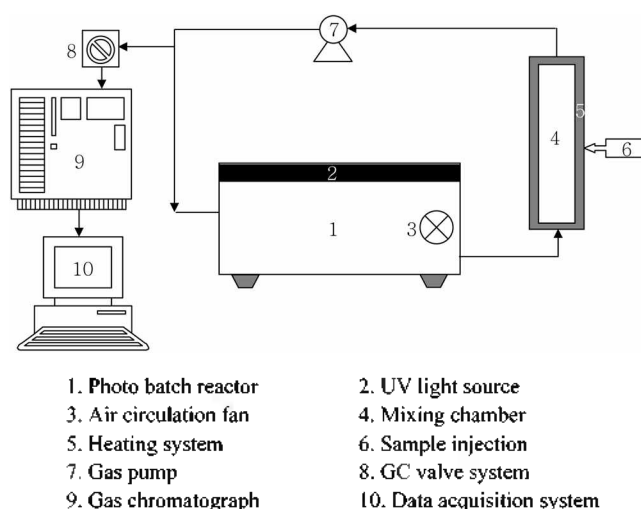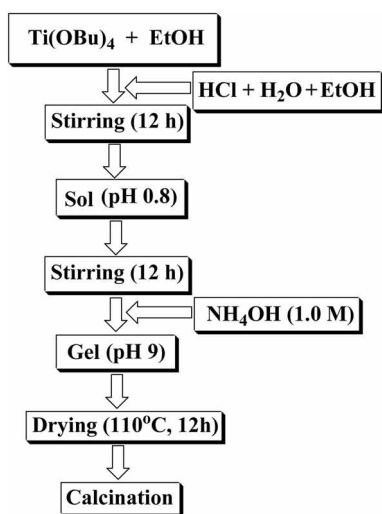

1. Photo batch reactor
2. UV light source
3. Air circulation fan
4. Mixing chamber
5. Heating system
6. Sample injection
7. Gas pump
8. GC valve system
9. Gas chromatograph
10. Data acquisition system

Figure 1. Schematic representation of the photoreactor and the experimental set-up.

Galaxy 7020A FT-IR spectrophotometer. The samples were ground with KBr pellets.

Photocatalytic degradation of toluene. All photocatalytic experiments were carried out using a photoreactor shown in Figure 1. The reactor is a double walled rectangular glass batch (400 × 210 × 192 mm) with the black outer wall and the transparent inner wall fused together. Inner walls are equipped with a UV lamp (Philips TUV 10W/G10 T8; λ_{max} = 254 nm) as light source at the top and a fan at the side for complete mixing of gases. A set of three Pyrex glass plates (each 270 × 50 × 5 mm) coated with photocatalyst were placed on a plastic stand (100 mm in height) in the reactor so that the distance between the light source and the Pyrex plates were 3 mm. Coating of the catalyst over the glass plates was carried out as follows: TiO₂ (0.50 g) was ground with a very dilute acetic acid solution to form a viscous homogenous paste. The paste was diluted by slow addition of water (1.0 mL) followed by addition of Triton X-100 (45 µL). The resulting paste was smeared on a glass substrate immobilized by an adhesive tape strip. After drying at 100 °C for 15 min, the film was annealed according to its calcination temperature for 30 min. The reactor was connected to a glass mixing chamber where the temperature was fixed at 70 °C to ensure the evaporation of toluene. The reactor was also connected to a Gas Chromatograph (GC-17A, Shimadzu) through a gas sampler system to monitor the toluene concentration at regular intervals. The GC was equipped with a HP-5 capillary column (30 m × 0.32 mm; Agilent Technologies). The injection and the column temperatures were 120 °C and 200 °C, respectively. The flame ionization detector was maintained at 250 °C. The reaction was started by injecting via micro-syringe the reactant toluene (7 mL) into the mixing chamber to be circulated by a peristaltic pump after evaporation and reach the gas-solid adsorption equilibrium. After the concentration of toluene was stabilized as monitored by GC, the UV lamp was turned on and the degradation of the toluene was recorded at a 30 min interval.

Ti(OBu)₄ + EtOH

↓⟵ HCl + H₂O + EtOH

Stirring (12 h)

↓

Sol (pH 0.8)

↓

Stirring (12 h)

↓⟵ NH₄OH (1.0 M)

Gel (pH 9)

↓

Drying (110°C, 12h)

↓

Calcination

Scheme 1

Results and Discussion

Synthesis. Scheme 1 describes our new synthetic strategy leading to the formation of mesoporous TiO₂ nanoparticles. A key feature of this method involves a gradual change in pH from 0.8 to 9.0 during the sol-gel transition. Namely, the initial transparent ethanolic solution of Ti(OBu)₄ turns into an opaque sol approximately 12 h after acid-catalyzed hydrolysis with a mixture of HCl/EtOH/H₂O. Viscosity of the resultant sol with pH < 1 increases gradually with further stirring for additional 12 h. A lot excess of solvent at such a low pH retard the condensation process and thus keep the sol in a stable state.[8] The formation of white gel was made possible by adjusting the pH of the reaction mixture to 9.0 through drop wise addition of NH₄OH. After aging for 2 h, syneresis or shrinkage of the gel takes place. The gel started contracted from the liquor due to the formation of oxygen bridges by the reaction of dandling bonds with each other forming the inorganic (TiOTi) network and expelling liquid from pores.[10] The overall process can be represented by the reaction represented in eqn. (1):

$$Ti(OBu)_4 \xrightarrow[24\ h\ /\ RT]{H^+/H_2O/EtOH} Ti(OH)_4 \xrightarrow{OH^-} \equiv Ti\!-\!O\!-\!Ti\equiv \quad (1)$$
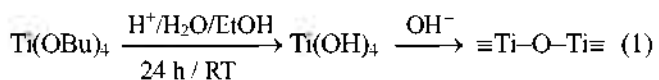
A large H₂O-to-Ti(OBu)₄ ratio together with a high acid concentration in the early stage of synthesis controls the rates of both hydrolysis and condensation; namely push the former reaction to completion to give Ti(OH)₄ before the latter starts. A unique advantage of these conditions is that anatase nanocrystals are generated as a sole crystalline phase.

Yet, as the pH increases, the condensation begins to accelerate to allow the formation of gel. High pH also contributes towards the stability of anatase phase by minimizing the possibility of the formation of multiphase TiO₂ known to take place at low pH.

All-in-all, our synthetic scheme employing a gradual change in pH demonstrates that the sol-gel transition can be well controlled and thus making a premeditated gelation possible. That is, the sol phase formed initially at low pH can remain intact from gelation that takes place only after base addition. Our additional observation is that the microstructure and physical properties of xerogels formed by our method are significantly different from those obtained from either acid- or base-catalyzed sol-gel method alone.

XRD analysis. The wide-angle XRD confirms that the anatase crystal phase (JCPDS 21-1272) is the one obtained predominantly under our experimental conditions as demonstrated in Figure 2. Line-broadening of the diffraction peak (101) revealed by the as-dried sample (T-ad) may be attributed to the small crystalline grain size (4.3 nm). The same peak becomes sharper and stronger as the calcination temperature increases, indicating an increase in crystallite size with higher crystallinity at least up to 600 °C. The Scherrer's formula was employed to estimate the crystallite sizes of T-ad through T-8 by measuring the full width at half-maximums (fwhms) of the (101) peaks centered at 25.36 ± 0.00667.[20] Both fwhms and peak centers were obtained by fitting the (101) peak to the Lorentzian function.

Table 1 shows the crystallite size of TiO₂ samples as a function of calcination temperature. The size ranges from 4.3 nm for T-ad (the smallest) to 45.5 nm for T-8 (the largest). The table also shows that the anatase phase of our samples is inert enough toward the anatase-rutile phase transformation at the temperature as high as 600 °C. The transition becomes almost complete (> 95%) at 800 °C as observed with T-8 (Figure 2 and Table 1). Consequently, these observations make it possible to remove bulk defects at high temperatures without accompanying serious phase transformation, responsible for low photocatalytic activity.

The SAXRD pattern of T-3 shows the mesoporous nature of the particles as confirmed by the presence of a broad band at 0.8° (2θ) with a d-spacing of 105 Å (Figure 3). The observation that this band has a long smooth tail extending
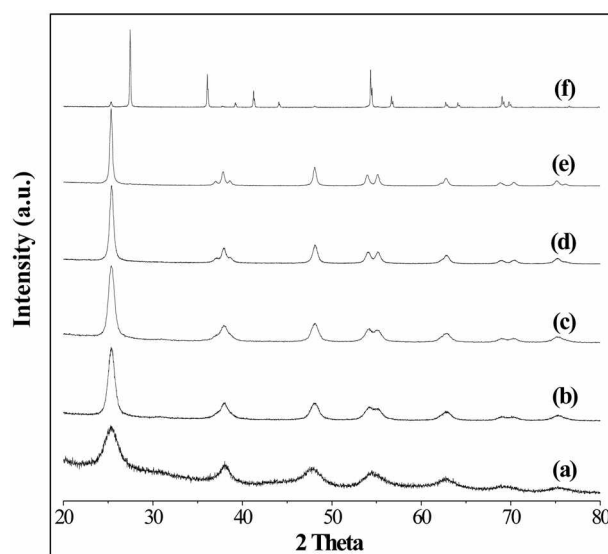

Figure 2. XRD patterns of TiO₂ samples; (a) as-dried, and calcined at (b) 350 °C, (c) 400 °C, (d) 500 °C, (e) 600 °C and (f) 800 °C.

Table 1. Some selected properties of TiO_2 powders

Catalyst	Crystal Phase[a]	Size of A (nm)[b]	S_{BET} (m²/g)[c]	V (cm³/g)[d]	D_{BJH} (nm)[e]
P-25	A:R (75:25)	25	50	–	–
T-ad	A	4.3	331	0.21	2.4
T-3	A	9	102	0.18	5.2
T-4	A	11	83	0.16	5.2
T-5	A	18	63	0.12	8.1
T-6	A:R (98:2)	29.6	27	0.08	12.5
T-8	A:R (5:95)	45.5	1.9	0.007	3.4

[a]Measured as content of anatase (%) = $\{I_A / I_A + 1.265I_R\} \times 100$. [b]Anatase crystallite size as measured by the Scherrer's equation. [c]Measured by BET method. [d]Pore volume taken from the volume of N_2 adsorbed at $P/P_o = 0.995$. [e]Average pore diameter estimated using desorption branch of the isotherm and the Barret-Joyner-Halenda (BJH) formula.

to approximately $2\theta = 4°$ supports the presence of only a short-range-ordered pore framework.[17,21,22] As expected this framework is sensitive on heating, *i.e.*, calcination as seen from the SAXRD pattern of T-5.[23,24] Here it is worth noting that mesoporosity can be achieved even without relying on the traditional sonochemical or micelle-template method.[25,26]

FT-IR studies. FT-IR spectroscopy may also be used to obtain some information about the effect of calcination on the nature of adsorbed species such as water and carboxylate. The IR spectra of T-ad and T-5 are shown in Figure 4. The spectrum of T-ad consists of bands assignable to the absorbed water: (i) the stretching in H_2O at 3,154 cm⁻¹; (ii) the bending in H_2O at 1,630 cm⁻¹; (iii) the stretching in Ti-O-Ti at 560 cm⁻¹; (iv) the carbonyl stretching in the carboxylate at 1401 cm⁻¹. The formation mechanism of the carboxyl needs further investigation. Upon calcination,
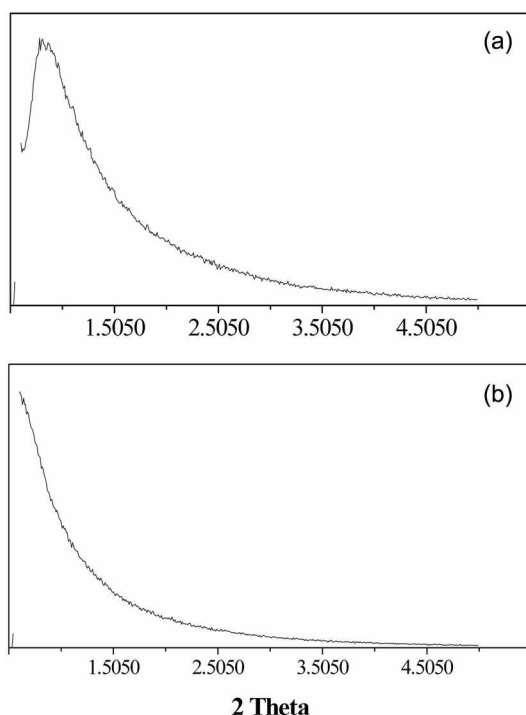
Figure 3. SAXRD patterns for TiO_2 samples calcined at; (a) 350 °C and (b) 500 °C.
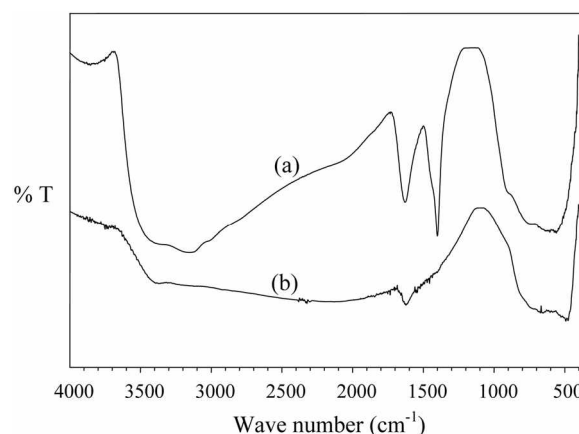
Figure 4. FT-IR spectra of TiO_2 samples; (a) as-dried and (b) calcined at 500 °C.

desorption of most of water and carboxylate must take place. This is reflected in the IR spectrum of T-5 which reveals a drastic decrease in the intensity for the corresponding bands. The only conspicuous band is the one due to the Ti-O-Ti stretching at 492 cm⁻¹.[27,28]

Nitrogen sorption analysis. Nitrogen adsorption-desorption isotherms of T-ad through T-8 are shown in Figure 5(a) to characterize their textural properties, pore sizes, and surface areas. BET surface areas and pore volumes are summarized in Table 1. As one might expect, the most general observation is that the surface area decreases as the calcination temperature increases. Quite naturally T-ad shows the highest surface area (331 m²g⁻¹) which can be explained in terms of the smallest particle size and the high mesoporosity. Yet, it must be acknowledged that the presence of coexistent amorphous phase in T-ad may also contribute to the high surface area. This negative effect of calcination on the surface area, however, is not as great with our samples as that observed with Degussa P-25. For instance, T-5 has BET of 63 m²g⁻¹ while Degussa P-25 shows 50 m²g⁻¹ at the same calcination temperature.

Isotherms with characteristic hysteresis loop (Type IV according to IUPAC classification of physisorption isotherms) throughout all samples but T-8 demonstrates their mesoporous nature. This loop is thought to be associated with the capillary condensation taking place in mesoporous solids. The single loop exhibited by each sample suggests a unimodel pore size distribution of type H4 in T-ad and H2 in others. The unique H4 loop found with T-ad can always be associated with narrow slit like pores although the H2 loop is difficult to interpret. The exhibition of H2 loop was once explained in terms of the mechanistic difference between condensation and evaporation processes occurring in pore.[8,29] The porosity (or the pore volume) also decreases with increase of the calcination temperature at high pressure ($P/P_o > ~0.6$).

Figure 5(b) shows plots of pore size distribution for our samples. Of five calcined samples, T-3 exhibits the smallest pore diameter (5.2 nm) with the narrowest pore size distribution (fwhm 2.5 nm). The pore size increases with
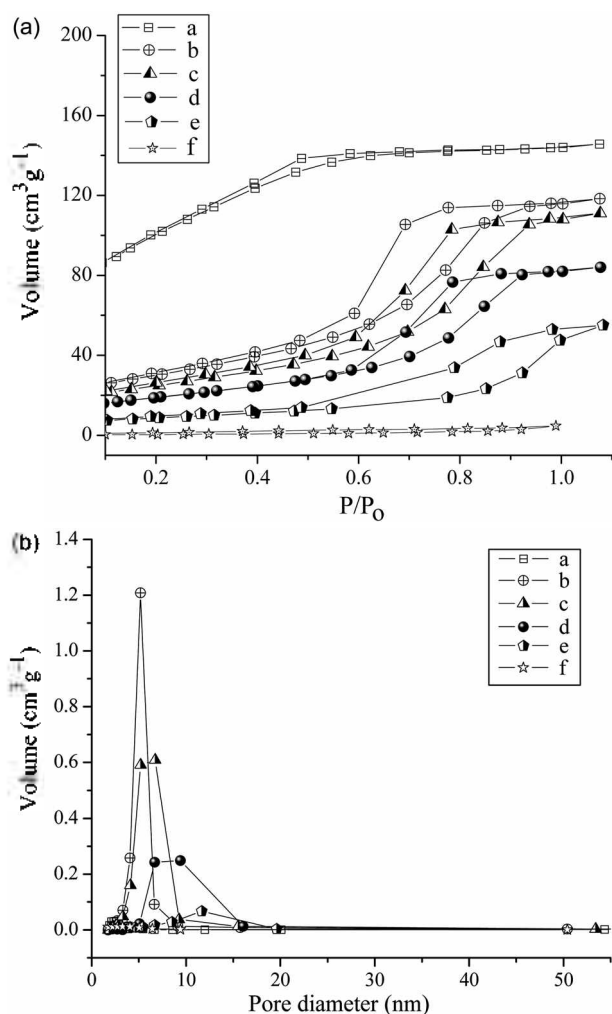
Figure 5. (a) N₂ adsorption-desorption isotherms and (b) BJH pore-size distribution of TiO₂ samples: (a) as-dried, and calcined at (b) 350 °C, (c) 400 °C, (d) 500 °C, (e) 600 °C and (f) 800 °C.

Figure 6. FE-SEM micrographs of TiO₂ samples; (a) calcined at 500 °C after grinding, (b, c) as-dried before grinding, (d) calcined at 350 °C before grinding.

concomitant widening of size distribution as the calcination temperature increases. T-5 and T-6, for example, exhibit the pore sizes of 8.1 and 12.3 nm with size distributions (fwhm) of 10.5 and 12.5 nm, respectively. Eventually they transform to non-porous rutile that is seen in T-8.

Morphology. The morphologies of the samples were determined by FE-SEM and HR-TEM. Figure 6 shows SEM micrographs of T-ad and T-5. While T-5 is obtained as agglomerates of various size distributions consisting of small and round particles (Figure 6a), Xerogels of T-ad before grinding, exist in the form of monoliths (Figures 6b and 6c). On calcination, however, thin layers of the solvent (EtOH) holding together a group of agglomerates through the hydrogen-bonding can readily escape, thus leaving behind pores (approximately 1.6 μm) on the surfaces of the monoliths. The resulting mesoporous structure is shown in Figure 6d.

Figure 7 shows highly magnified TEM images of T-ad, T-3, and T-5, each of which reveals well-resolved crystalline planes with d-spacing of 3.5 Å, demonstrating the presence of [101] plane of anatase. The figure shows a high degree of
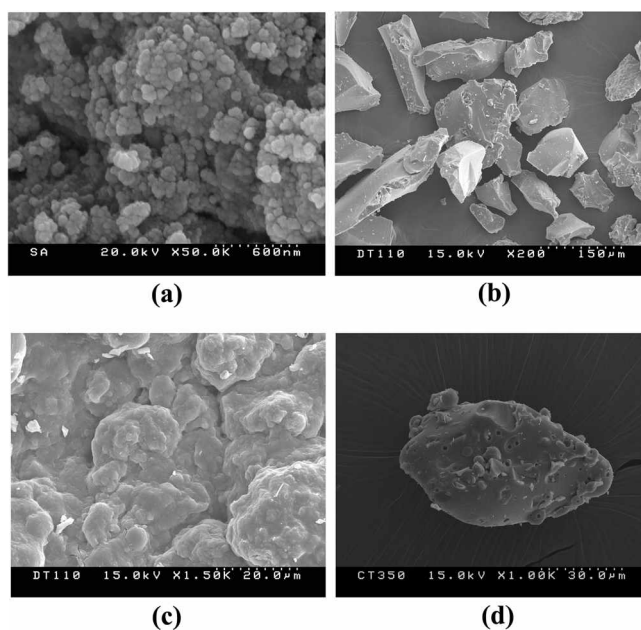
aggregation in T-ad, T-3, and T-5. T-ad possesses good crystallinity with a diameter in the range of 4-5 nm (Figs. 7a, b). These results are in good agreement with those obtained from its XRD patterns (Fig. 2). T-3 and T-5 have diameters 7-9 and 15-18 nm, respectively. These values can also be estimated from their corresponding XRD patterns. No long-range order mesoporous structure was observed, which may also be expected from the low-angle XRD results. In conclusion, the mesoporosity is mainly due to the interparticle porosity.

Thermal characteristics. Figure 8 shows TG and DTA analyses of T-ad. The degradation takes place in three well-differentiated steps. The maximum weight loss occurs at around 100 °C due to sample dehydration. The first phase of degradation takes place at 50-150 °C, which is attributable to the elimination of physically adsorbed water and alcohol. A broad endothermic DTA curve centers at around 120 °C. The second phase of degradation starts at 150 °C and continues up to 350 °C. This corresponds to the burning of residual organic material and chemically adsorbed water. This is also revealed by an exothermic DTA curve (curve maximum at 330 °C). The curve remains steady in the temperature range 350-800 °C and thus showing no significant weight loss.

Surface properties. The XPS of T-5 was taken to garner additional information concerning the nature of the phase. Figure 9 shows two characteristic peaks at 459.7 and 465.5 eV assignable to Ti-2p₃/₂ and Ti 2p₁/₂, respectively. These patterns are very similar to those of typical Ti⁴⁺-anatase phase. The O 1s photoelectron peak can be resolved into two components by Gaussian curve fitting technique, enabling us to assign two peaks 530.8 and 533.4 eV to lattice oxygen and adsorbed oxygen (or water), respectively. The binding
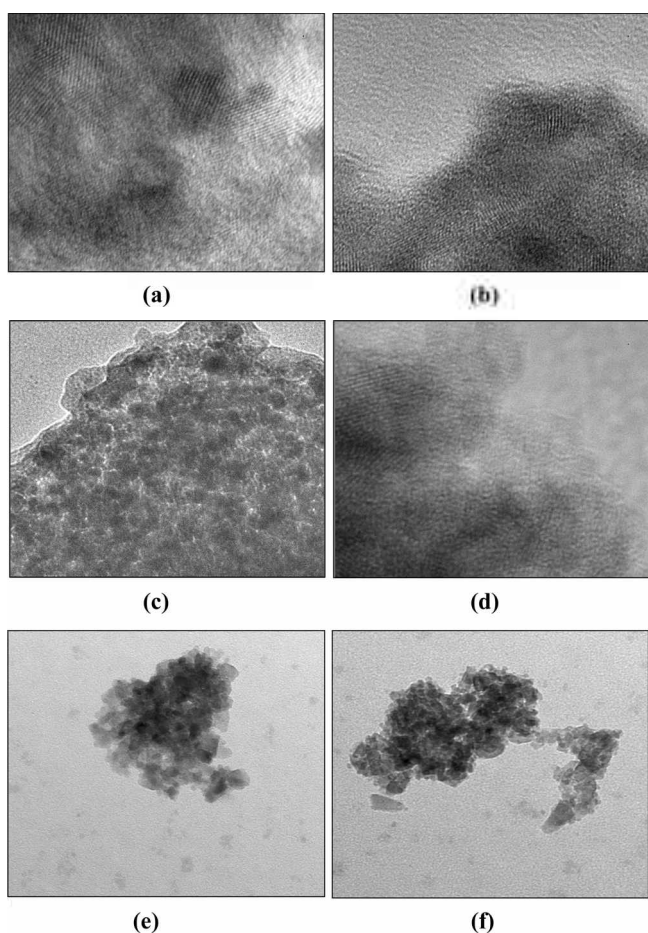
Figure 7. TEM micrograph of TiO_2 samples, (a, b) as-dried, and calcined at (c, d) 350 °C and (e, f) 500 °C.
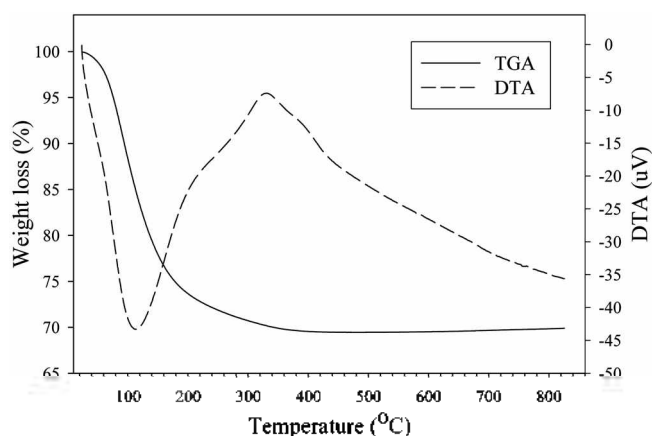

Figure 8. TGA analysis of as-dried TiO_2.

Figure 9. XPS analysis of TiO_2 sample calcined at 500 °C.

Figure 10. Catalytic degradation of toluene by different TiO_2 samples; (a) blank, (b) P-25, (c) as-dried, and calcined at (d) 350 °C, (e) 400 °C, (f) 500 °C and (g) 600 °C.

energy values of C (1s) at 286.2 and 288.3 eV are due to the presence of C-O and -C=O, respectively.[30,31] Regarding the presence of these peaks, it is worth noting that a certain amount of alkoxide always remains as impurity to be converted later to surface-adsorbed carbon or oxides of carbon on calcination.

Catalytic activity. With a series of mesoporous TiO_2 in hand, we have performed photodegradation of toluene under UV to benchmark their catalytic efficiencies (Figure 10). For
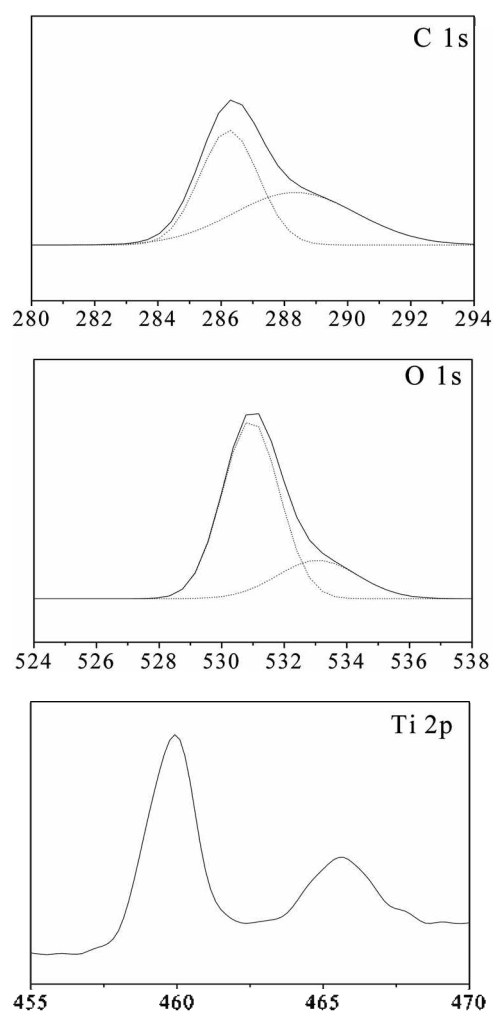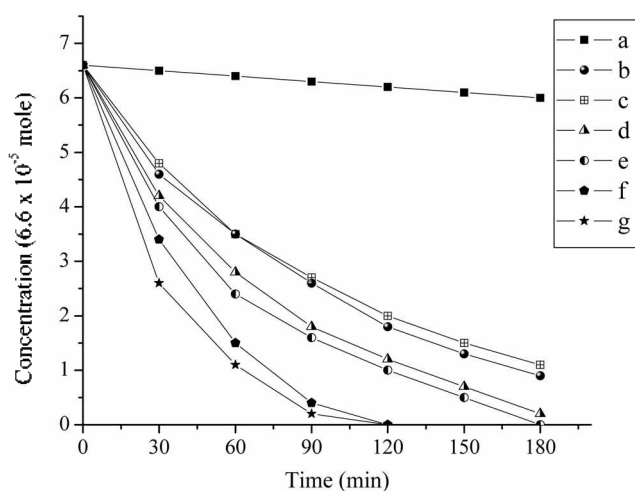
comparative purposes, commercially available Degussa P-25 was also employed as catalyst. Indeed, all but T-ad in the series push the reaction into completion within 2-3 h, following the first order kinetics. The reaction rate reaches

as high as 3.9×10^{-2}/min with T-6, which exceeds the rate with the commercially available Degussa P-25 by a factor of 3.2.

Figure 10 shows that T-ad exhibits the photocatalytic activity comparable to that of P-25. Two factors may be responsible for the activity of anatase T-ad. They are: (1) a very surface area (331 m^2g^{-1}); (2) the mesoporous structure enabling more active sites to adsorb reactant molecules. One may argue, however, that the high surface area of T-ad causes adsorption of toluene more readily than decomposition.

Yet, this proves not to be the case, as observed with other catalysts in the series such as T-3, T-4, T-5, and T-6. T-3, for example, exhibits even higher reactivity than P-25 in spite of smaller surface area (102 m^2g^{-1}) than that of T-ad. This observation clearly demonstrates that decomposition of toluene is mainly due to increased crystallinity as a result of calcination. In accordance with this statement, the catalytic activity increases in the following order: T-ad < T-3 < T-4 < T-5 < T-6 (Figure 10). Namely, catalytic activity increases with increase in crystallinity in spite of decrease in the surface area or the pore volume. Parallel observations such as these are elsewhere in the literature.[2,32]

In particular, the relationship between the photocatalytic activity and crystallinity has recently been delved in detail by Inagaki.[33] Their observations are that crystallinity as well as the crystal size increases with an increase in calcination temperature. The crystal size in turn decreases the lattice strain of anatase, thus ultimately retarding the electron-hole recombination ($e^−$-h^+). The highest activity exhibited by T-6 agrees well with the above-mentioned observations. Finally, our catalysts are not only active but also highly recyclable to show little catalytic deactivation after repeated use for 3-4 times.

Conclusions

A novel acid-base catalyzed synthesis leading to the formation of a series of mesoporous crystalline TiO₂ is described. Our synthetic approach not only excludes the use of the traditional template and sonochemical methods but also guarantees the exclusive formation of the anatase phase possessing certain properties essential for high catalytic activity: nano-crystallinity; large surface area; thermal stability.

The physicochemical properties of the particles in the series were characterized by various spectroscopic and analytical techniques. The photocatalytic oxidation of toluene under UV-irradiation follows first order kinetics. The reaction rate reaches as high as 3.9×10^{-2}/min which exceeds the rate with the commercially available Degussa P-25 by a factor of 3.2. When comparison is made among the catalysts T-3 through T-6, the reactivity increases with increase in the calcination temperature which in turn increases the crystallinity of the anatase phase, thus revealing the following rate orders: T-3 < T-4 < T-5 < T-6.

References

1. Hoffmann, M. R.; Martin, S. T.; Choi, W.; Bahnemann, D. W. *Chem. Rev.* **1995**, *95*, 69.
2. *Photocatalysis Science and Technology*; Kaneko, M.; Okure, I., Eds.; Springer-Verlag: New York, 2002; pp 29-47.
3. Mills, A.; Porter, G. *J. Chem. Soc. Faraday Trans.* **1982**, *78*, 3659.
4. Bickley, R. I.; Gonzalez-Carreno, T.; Lees, J. S.; Palmisano, L.; Tilley, R. J. D. *J. Solid-State Chem.* **1991**, *92*, 178.
5. Ohtani, B.; Zhang, S.-W.; Nishimoto, S.-I.; Kagiya, T. *J. Photochem. Photobiol. A* **1992**, *64*, 223.
6. Sclafani, A.; Palmisano, L.; Schiavello, M. *J. Phys. Chem.* **1990**, *94*, 829.
7. Chen, M.-L.; Bae, J.-S.; Oh, W.-C. *Bull. Korean Chem. Soc.* **2006**, *27*, 1423.
8. *Sol-Gel Science: The Physics and Chemistry of Sol-Gel Processing*; Brinker, C. J.; Scherer, G. W., Eds.; Academic Press: Boston, 1990.
9. Pecchi, G.; Reyes, P.; Lopez, T.; Gomez, R.; Moreno, A.; Fierro, J. L. G. *J. Chem. Technol. Biotechnol.* **2002**, *77*, 944.
10. Yoldas, B. E. *J. Mater. Sci.* **1986**, *21*, 1087.
11. Barringer, E. A.; Bowen, H. K. *J. Am. Ceram. Soc.* **1982**, *65*, 199.
12. Montoya, I. A.; Viveros, T. J.; Dominguez, M.; Canales, L. A.; Schifter, I. *Catal. Lett.* **1992**, *15*, 207.
13. Ding, X.-Z.; Liu, X.-H. *Materials Science and Engineering A* **1997**, *224*, 210.
14. Ward, D. A.; Ho, E. I. *Ind. Eng. Chem. Res.* **1995**, *34*, 421.
15. Terabe, K.; Kato, K.; Miyazaki, H.; Yamaguchi, S.; Imai, A.; Iguchi, Y. *J. Mater. Sci.* **1994**, *29*, 1617.
16. Song, K. C.; Pratsinis, S. E. *J. Am. Ceram. Soc.* **2001**, *84*, 92.
17. Bose, F.; Ayral, A.; Albouy, P.-A.; Guizard, C. *Chem. Mater.* **2003**, *15*, 2463.
18. Yu, J.; Su, Y.; Cheng, B.; Zhou, M. *J. Mol. Catal. A: Chemical* **2006**, *258*, 104.
19. Sakthivel, S.; Hidalgo, M. C.; Bahnemann, D. W.; Geissen, S.-U.; Murugesan, V.; Vogelpohl, A. *Applied Catalysis B: Environmental* **2006**, *63*, 31.
20. *Elements of X-ray Diffraction*, 2nd ed.; Cullity, B. D., Ed.; Addison-Wesley: Reading, 1978; p 102.
21. Wang, H.; Miao, J.-J.; Zhu, J.-M.; Ma, H.-M.; Zhu, J.-J.; Chen, H.-Y. *Langmuir* **2004**, *20*, 11738.
22. Wang, Y.; Chen, S.-G.; Tang, X.-H.; Palchik, O.; Zaban, A.; Gedanken, A. *J. Mater. Chem.* **2001**, *11*, 521.
23. Antonelli, D. M. *Micropor. Mesopor. Mater.* **1999**, *30*, 315.
24. Wang, X.; Yu, J. C.; Ho, C.; Hou, Y.; Fu, X. *Langmuir* **2005**, *21*, 2552.
25. Wang, Y.; Tang, X.; Yin, L.; Huang, W.; Hacohen, Y. R.; Gedanken, A. *Adv. Mater.* **2000**, *12*, 1183.
26. Yang, P.; Zhao, D.; Margolese, D. I.; Chmelka, B. F.; Stucky, G. D. *Chem. Mater.* **1999**, *11*, 2813.
27. Peiro, A. M.; Peral, J.; Domingo, C.; Momenech, X.; Ayllon, J. A. *Chem. Mater.* **2001**, *13*, 2567.
28. Biniak, S.; Szymanski, G.; Siedlewski, J.; Swiatkowski, A. *Carbon* **1799**, *35*, 810.
29. Sing, K. S. W.; Everett, D. H.; Haul, R. A. W.; Moscou, L.; Pierotti, R. A.; Rouquerol, J.; Siemieniewska, T. *Pure and Applied Chemistry* **1985**, *57*, 603.
30. Yu, J.; Zhao, X. *Mater. Res. Bull.* **2000**, *35*, 1293.
31. Patil, K. R.; Sathaye, S. D.; Khollam, Y. B.; Deshpande, S. B.; Pawaskar, N. R.; Mandale, A. B. *Mater. Lett.* **2000**, *57*, 1775.
32. Linsebigler, L. A.; Lu, G.; Yates, T. J. *Chem. Rev.* **1995**, *95*, 735.
33. Inagaki, M.; Nonaka, R.; Tryba, B.; Morawski, A. W. *Chemosphere* **2006**, *64*, 437.